Zero-field quantum sensing via precise geometric controls for a spin-1 system

Zhijie Li,[1,2,§] Xiangyu Ye,[1,2,§] Xi Kong,[3,*] Tianyu Xie,[1,2] Zhiping Yang,[1,2] Pengju Zhao,[1,2] Ya Wang,[1,2,4] Fazhan Shi,[1,2,4,5,†] and Jiangfeng Du[1,2,4,6,‡]

[1] *CAS Key Laboratory of Microscale Magnetic Resonance and School of Physical Sciences, University of Science and Technology of China, Hefei 230026, China*

[2] *CAS Center for Excellence in Quantum Information and Quantum Physics, University of Science and Technology of China, Hefei 230026, China*

[3] *The State Key Laboratory of Solid State Microstructures and Department of Physics, Nanjing University, Nanjing 210093, China*

[4] *Hefei National Laboratory, University of Science and Technology of China, Hefei 230088, China*

[5] *School of Biomedical Engineering and Suzhou Institute for Advanced Research, University of Science and Technology of China, Suzhou 215123, China*

[6] *School of Physics, Zhejiang University, Hangzhou 310027, China*

(Received 12 February 2023; revised 17 February 2024; accepted 17 April 2024; published 6 May 2024)

The presence of an external magnetic field leads to the loss of anisotropic physical information and is responsible for the broadening of spectra in sensing experiments with solid-state quantum sensors. However, the range of applicable sensing protocols at zero field was limited due to the incomplete manipulations. Here we propose and demonstrate a precise geometric control protocol in a spin-1 quantum sensor for zero-field multiquantum gates. By employing specific phased geometric controls, state leakage is prevented at zero field even under low control power, which allows much more complicated multipulse control especially under living biological conditions. Our method offers an approach to implement an arbitrary multiquantum gate on the spin-1 quantum sensor, rendering it a valuable tool for zero-field multipulse quantum technologies, such as nanoscale zero-field multidimensional nuclear magnetic resonance.

DOI: 10.1103/PhysRevApplied.21.054011

I. INTRODUCTION

In recent years, significant progress has been made in quantum sensing techniques based on controllable quantum systems. One successful example is the nitrogen-vacancy (N-V) center in diamond, which possesses numerous merits, including nanoscale size, biocompatibility, and long coherence time under ambient conditions [1–5]. Typically, solid-state quantum sensors require a static external magnetic field to lift the degeneracy of their ground-state manifolds. However, the presence of an external magnetic field suppresses the anisotropic interactions within the target sample, resulting in the loss of anisotropic physical information and causing inhomogeneous spectral broadening. Hence, by developing zero-field techniques based on magnetic resonance, high spectral resolution is achievable, which can enhance detection sensitivity and reveal material information previously unobservable. A well-known zero-field technique is the zero- to ultralow-field nuclear magnetic resonance (ZULF NMR) spectroscopy. This technique effectively mitigates the inhomogeneous broadening of the spectrum induced by dipolar couplings and quadrupolar couplings [6–8]. More zero-field scenarios can be found in the field of electromagnetic biology [9,10] and in the research of ferromagnetic film magnetization [11]. However, practical zero-field techniques in the room-temperature solid-state magnetic sensors still lag behind the thriving applications with an external field, particularly in the field of nanoscale to single-molecule nuclear magnetic resonance [12,13]. One major challenge is the difficulty in achieving precise control due to state leakage, which hinders the implementation of complex control techniques comparable to those used in high-field applications. In order to extend the zero-field condition to solid-state quantum sensors like N-V centers, it is crucial to implement accessible high-fidelity quantum control for the spin-1 system.

To address the near-degenerate quantum states in the absence of external fields, one approach is to employ circularly polarized microwave pulses [14,15]. While this method is effective when using a few pulses, it is limited in its ability to utilize double quantum (DQ) transitions with a multipulse method, which is crucial for sensing weak

*Corresponding author: kongxi@nju.edu.cn
†Corresponding author: fzshi@ustc.edu.cn
‡Corresponding author: djf@ustc.edu.cn
§These authors contributed equally to this work.

ac signals. Recent works have paved the way for realizing dynamical decoupling (DD) with linearly polarized microwave pulses at zero field by manipulating the three-level system (3LS) via an effective Raman coupling [16]. This method enables the utilization of high-power multiple pulses, leveraging the advantage of DQ transitions at zero field to offer a significantly broader sensing bandwidth and expanded sensitivity range. However, the effectiveness of this method is compromised by the occurrence of state leakage due to the contradiction between the unavoidable hyperfine nondegeneracy and the limited driving field strength [17,18]. Subsequently, sequences that counteract the effects of the nondegeneracy detuning were proposed [19]. All these methods are sufficient for performing measurements in a Ramsey or DD manner. However, they lack the versatility needed for designing complex sequences, including those that correlate different transitions, which is a critical requirement in quantum sensing with complicated control protocols such as two-dimensional NMR [20–22]. In this study, we introduce a method for conducting arbitrary unitary operations within the dynamical subspace of a 3LS. This scheme effectively prevents state leakage even when using a relatively weak driving field by harnessing the geometric properties of the dressed states compared to previous methods. Through this approach, we can achieve a collection of effective DQ rotation operations. We have demonstrated a zero-field quantum sensing scheme utilizing single N-V centers based on the proposed method, which includes DD and correlation spectroscopy.

II. GEOMETRIC CONTROL SCHEME

A single N-V center in diamond consists of a substitutional nitrogen and a neighboring vacancy, its electron ground states form a typical 3LS [Fig. 1(a)]. The Hamiltonian of a single N-V center can be given by ($\hbar = 1$) [19,23]

$$H = (D + d_{\parallel}\Pi_z)S_z^2 + (\Delta + \delta I_z)S_z + d_{\perp}[\Pi_x(S_y^2 - S_x^2) + \Pi_y(S_xS_y + S_yS_x)], \quad (1)$$

where $S_{x,y,z}$ is the spin-1 operator, D is the zero-field splitting, $d_{\parallel}$ and $d_{\perp}$ are the longitudinal and transverse electric dipole moment components, Δ refers to the Zeeman splitting induced by the external magnetic field along the N-V center's principle axis, δ contains hyperfine couplings with the surrounding spin-1/2 nuclei I, and $\mathbf{\Pi} = (\Pi_x, \Pi_y, \Pi_z)$ denotes the total effective electric field. A linearly polarized microwave field $\Omega\cos(\omega t + \phi)S_x$ is applied, which simultaneously drives oscillations between the states $|0\rangle \leftrightarrow |+1\rangle$ and $|0\rangle \leftrightarrow |-1\rangle$. This leads to the emergence of an effective driving between the states $|+1\rangle$ and $|-1\rangle$ [Fig. 1(a)] and results in dressed states $|+\rangle = (|+1\rangle + |-1\rangle)/\sqrt{2}$ and $|-\rangle = (|+1\rangle - |-1\rangle)/\sqrt{2}$ in the interaction picture.

By utilizing phase-fixed geometric controls [16–19], it is possible to accumulate a geometric π phase on the state $|+\rangle$ while keeping the state $|-\rangle$ nearly unchanged, as long as the 2π cycle occurs rapidly compared to the detuning modulation [Fig. 1(b)]. This approach enables the realization of a nearly π pulse within the $\{|+1\rangle, |-1\rangle\}$ subspace. However, the presence of the hyperfine coupling δ and the transverse effective electric field (Π_x, Π_y) can induce state leakage to the $|0\rangle$ state. The imperfect controls in the dynamical decoupling sequence result in degraded spin coherence and distorted signal filtering. As a consequence, this decreases the sensitivity and makes it difficult to implement complex multipulse quantum sensing protocols.

Here we introduce a precise geometric control method that prevents state leakage and enables a diverse range of operations. With the resonance condition $\omega = D + d_{\parallel}\Pi_z$ and the microwave polarization perpendicular to the transverse projection of $\mathbf{\Pi}$, the effective Hamiltonian of the system can be expressed as

$$H_1(\Omega, \phi) = \left(\frac{\Omega e^{i\phi}}{2}|0\rangle + \frac{\delta' e^{i\psi}}{2}|-\rangle\right)\langle +| + \text{H.c.}, \quad (2)$$

where $\delta' = \sqrt{\delta^2 + 4d_{\perp}^2\Pi_y^2}$ and $\psi = \arctan\left(-2d_{\perp}\Pi_y/\delta\right)$. When $\Omega = \delta'$ [Fig. 1(c)], a complete transition from state $|0\rangle$ to state $|-\rangle$ is possible with an appropriate evolution time. Defining $|\phi'\rangle = (e^{i\phi}|0\rangle + e^{i\psi}|-\rangle)/\sqrt{2}$, the effective Hamiltonian Eq. (2)

$$H_1(\delta', \phi) = \frac{\delta'}{\sqrt{2}}\left(|\phi'\rangle\langle +| + |+\rangle\langle\phi'|\right) \quad (3)$$

is proportional to the Pauli-X matrix of the pseudospin spanned by the $\{|+\rangle, |\phi'\rangle\}$ basis. By applying a 2π rotation $U_{\phi} = e^{-iH_1(\delta',\phi)T'}$ to the pseudospin for a duration $T' = \sqrt{2}\pi/\delta'$ [Fig. 1(c)], an overall phase is introduced in the $\{|+\rangle, |\phi'\rangle\}$ subspace [17,24]. Note that the orthogonal state $|\phi'_{\perp}\rangle = (e^{i\phi}|0\rangle - e^{i\psi}|-\rangle)/\sqrt{2}$ to the subspace remains unchanged [Fig. 1(a)]. The operation U_{ϕ} introduces conjugate phase factors in the $\{|0\rangle, |-\rangle\}$ subspace [Fig. 1(d)], i.e.,

$$U_{\phi} = -e^{-i(\phi-\psi)}|-\rangle\langle 0| - e^{i(\phi-\psi)}|0\rangle\langle -|. \quad (4)$$

Consequently, the composite pulse defined as $G_{\pi}^{\phi} = U_{\phi}U_{\phi+\pi}$ precisely leads to $|+\rangle \to |+\rangle$ and $|-\rangle \to -|-\rangle$ [Fig. 1(e)], and the spin-flip pulse in the $\{|+1\rangle, |-1\rangle\}$ subspace can be achieved without any leakage to the state $|0\rangle$, resulting in the zero-field dynamical decoupling (ZDD) sequence with equally spaced G_{π}^{ϕ} operations.

Generally, the phased geometric gate $G_{\theta}^{\phi} = U_{\phi}U_{\phi+\theta}$ is equivalent to the rotation operator along z axis in the

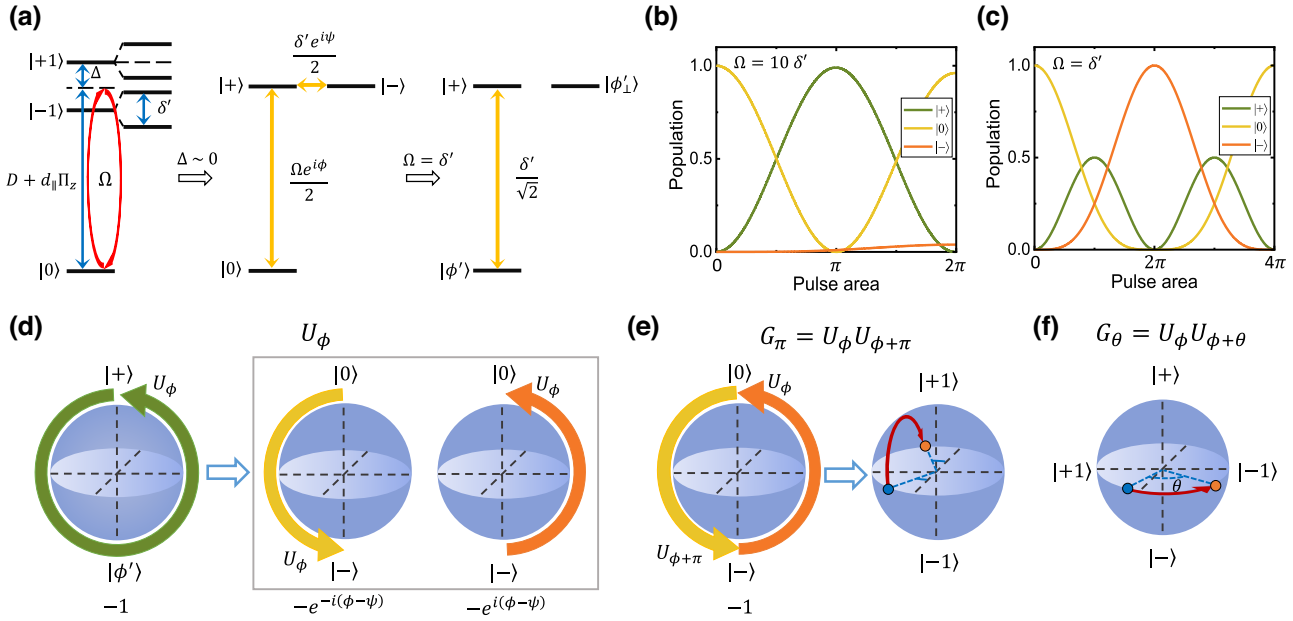

FIG. 1. Illustration of phased geometric control protocol. (a) The spin triplet of the electronic ground state of N-V centers. When the system is driven by a linearly polarized microwave pulse with amplitude Ω, angular frequency $\omega = D + d_\parallel \Pi_z$ and phase ϕ, Rabi oscillations $|0\rangle \leftrightarrow |-1\rangle$ and $|0\rangle \leftrightarrow |+1\rangle$ are activated simultaneously (left). Transformed to the $|0\rangle$, $|+\rangle = (|+1\rangle + |-1\rangle)/\sqrt{2}$ and $|-\rangle = (|+1\rangle - |-1\rangle)/\sqrt{2}$ basis, an effective Raman coupling is revealed (middle). When the driving power Ω is set to δ', the coupling exists only between $|+\rangle$ and $|\phi'\rangle$ states, where $|\phi'\rangle = (e^{i\phi}|0\rangle + e^{i\psi}|-\rangle)/\sqrt{2}$ is defined by the microwave phase ϕ and a coupling determined phase ψ, and $|\phi'_\perp\rangle = (e^{i\phi}|0\rangle - e^{i\psi}|-\rangle)/\sqrt{2}$ is the orthogonal counterpart to $|\phi'\rangle$ (right). (b) Evolution of the states driven with $\Omega = 10\,\delta'$. The oscillation in the $\{|0\rangle, |+\rangle\}$ geometric qubit space dominates in the 3LS, while the transition to the state $|-\rangle$ is strongly suppressed in one cycle. (c) Evolution of the states driven with $\Omega = \delta'$. The complete transition between the states $|0\rangle$ and $|-\rangle$ can be realized, and the shortest pulse for a complete transition in the $\{|0\rangle, |-\rangle\}$ subspace corresponds to the 2π pulse in the $\{|+\rangle, |\phi'\rangle\}$ subspace. (d) Schematic diagram of the 2π operation U_ϕ. The phase factors of final states brought by U_ϕ are shown below each corresponding Bloch sphere. (e) Schematic diagram of the phased geometric gate operation $G_\pi = U_\phi U_{\phi+\pi}$. The state $|+\rangle$ undergoes a 4π cycle when G_π is applied, which results in a phase factor valued $+1$. The G_π operation brings a phase factor valued -1 in the $\{|0\rangle, |-\rangle\}$ subspace (left), and the effect of G_π on the dynamical qubit is equivalent to that of a π pulse (right), where the blue spot and the orange spot in the sphere represent the initial state and the final state, respectively. (f) The effect of the operation $G_\theta = U_\phi U_{\phi+\theta}$. G_θ is equivalent to an effective rotation along z axis in the $\{|+\rangle, |-\rangle\}$ subspace.

$\{|+\rangle, |-\rangle\}$ subspace, and the effect of G_θ^ϕ is depicted as a rotation on the Bloch sphere [Fig. 1(f)]. Combined with the free evolution, which rotates the state vector along the horizontal axis due to the hyperfine interaction, arbitrary effective rotation in the $\{|+\rangle, |-\rangle\}$ subspace can be implemented. For quantum sensing purposes, in addition to the $G_{\pm\pi}^\phi$ gates that implement DD, the $G_{\pm\pi/2}^\phi$ gates are particularly relevant due to their ability to convert coherence into state population in the $\{|+1\rangle, |-1\rangle\}$ basis, which can be used to obtain correlation of phases accumulated in separate DD sequences. These capabilities of the phased geometric gates pave the way for intricate sensing applications at zero field, such as multidimensional NMR.

III. PHASED GEOMETRIC GATE

The polarization direction of the applied transverse microwave field is calibrated to be perpendicular to the transverse effective electric field vector in order to ensure equal transition probabilities for the two single quantum transitions depicted in Fig. 1(a). The polarization direction is defined as the x axis. For N-V centers containing a native adjacent ^{15}N atom, the value of δ is primarily determined by the intrinsic ^{15}N hyperfine interaction $A_\parallel$. Consequently, the resulting nondegenerate splitting can be calculated as $\delta' = \sqrt{A_\parallel^2 + 4d_\perp^2 \Pi_y^2} = 2\pi \times 3.04(1)$ MHz. Therefore, the amplitude and the angular frequency of the manipulating microwave field can be determined by $\Omega = \delta'$ and $\omega = D + d_\parallel \Pi_z = 2\pi \times 2870.79(1)$ MHz. By setting $\phi = 0$, the $|+\rangle \leftrightarrow |0'\rangle$ transition is driven with the angular frequency of $\overline{\Omega} = \sqrt{\delta'^2 + \Omega^2} = \sqrt{2}\delta'$, and the pulse length of a unit operation U_ϕ is defined by $T' = 2\pi/\overline{\Omega}$ [Fig. 2(a)]. The phased geometric gate $G_\theta^\phi = U_\phi U_{\phi+\theta}$ is implemented using two-unit operations with phase difference θ. Multipulse quantum sensing protocols can be realized by employing θ values required by specific operations.

Simply using two separate operations, $U_0 - \tau - U_0$, the Ramsey sequence can be implemented with the variation

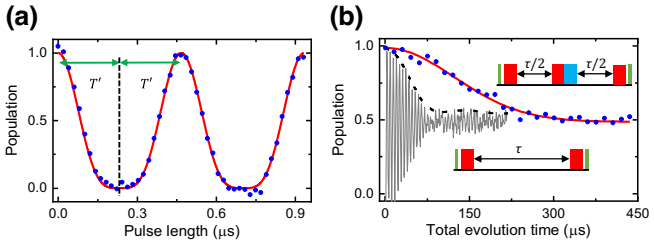

FIG. 2. The state evolution under continuous driving field and pulsed experiments. (a) The population of the state $|0\rangle$ under the continuous driving field with different durations. The N-V spin state is initialized and read out using 532-nm laser pulses. A microwave field with an angular frequency of $\omega = D + d_{\parallel}\Pi_z$ is applied. A complete transition to $|-\rangle$ can be realized when $\Omega = \delta'$ is met, and a microwave pulse with a duration of $T' = 233.5$ ns corresponds to a 2π pulse in the $\{|0\rangle, |+\rangle\}$ subspace. (b) Ramsey interference and spin echo. The Ramsey sequence is conducted with two separate 2π pulses. The observed data (gray line) exhibits an undersampled oscillation with a frequency of $\delta'/2\pi$. The envelope of the oscillation (black dashed line) is fitted using the function $\cos(\omega t)\exp[-(t/T_2^*)^p]$ and yields a dephasing time $T_2^* = 120(2)$ μs $[p = 1.8(1)]$ in the $\{|+1\rangle, |-1\rangle\}$ basis. The Ramsey and the spin-echo sequences are depicted, the spin-echo sequence features a 4π pulse in the middle of the Ramsey sequence. This 4π pulse is composed of two 2π pulses, one phased 0 (red rectangle) and the other phased π (blue rectangle). The decoherence time under the echo sequence is evaluated using the function $\exp[-(t/T_2)^p]$ with $T_2 = 173(9)$μs $[p = 2.0(1)]$ (red line).

of the free evolution time τ. By performing the Ramsey sequence, oscillation at a frequency of $\delta'/2\pi$ emerges [Fig. 2(b)]. This oscillation is specific to this zero-field Ramsey fringe. The envelope of this oscillation reflects the environmental information of the qubit and directly reveals the decoherence within the $\{|+1\rangle, |-1\rangle\}$ subspace. The fitted dephasing time is $T_2^* = 120(2)$ μs. The Hahn-echo sequence is achieved by inserting the phased geometric gate G_{π}^{ϕ} in the middle of the Ramsey sequence. This G_{π}^{ϕ} operation enables a flip between the two phase-accumulating states. By employing the zero-field Hahn-echo, low-frequency environmental noise is suppressed, leading to the restoration of coherence [Fig. 2(b)]. The fitted decoherence time is $T_2 = 173(9)$ μs.

IV. ZERO-FIELD SENSING PROTOCOL

We successfully implement the ZDD-N sequence, a multipulse quantum sensing protocol, by performing precise operations following the form of $U_0 - (\tau/2 - G_{\pi}^0 - \tau - G_{-\pi}^0 - \tau/2)^{N/2} - U_0$ [Fig. 3(a)], where $N(\tau + 2T') = NT$ represents the total evolution time, T is the interval of the center of two adjacent gates. The interlaced sequence is specifically designed to compensate for the fidelity degradation arising from pulse imperfections up to the second order [19,25,26]. When applying the ZDD-N sequences, we observe a substantial prolongation of DQ coherence within the subspace as the pulse number N increases [Fig. 3(b)]. The coherence time reaches near saturation at $N = 64$ with $T_2 = 1.06(8)$ ms, indicating that the manipulation fidelity and the coherence resource are sufficient for multipulse quantum sensing protocols. An artificial ac signal with a frequency of $f = 0.5$ MHz are observed and shown in Fig. 3(c). The observed frequency is $f' = 1/(2T_s) = 0.499(1)$ MHz, corresponding to the coherence dip at $T_s = 1.002(1)$ μs [Fig. 3(c)]. The dynamical decoupling protocol shown here is crucial for diverse sensing purposes.

To implement the zero-field correlation spectroscopy sequence for multidimensional NMR, $G_{\pi/2}^0$ gates are inserted between the two separate ZDD sequences as shown in Fig. 3(d). These gates are applied immediately after or before the phase-accumulating sectors to convert phase differences into population or vice versa. The lowest-order correlation reveals the signal frequency [27], as $\langle \sin\psi_1 \sin\psi_2 \rangle \sim \cos(2\pi f\,(2\tau + t))$, where τ is set to $T_s - 2T'$ according to the coherence dip in the ZDD spectrum, ψ_i is the phase accumulated during each individual ZDD sequence. The correlation signal of two ZDD-16 sequences for the artificial ac field is shown in Figs. 3(e) and 3(f). This demonstrates that our method can be used for complex quantum sensing tasks.

V. EVALUATION OF FIDELITY

The performance of different zero-field DD sequences at the same power level was compared. The fidelity of the ZDD-4 and the LDD-4 [19] sequences with driving power δ' is depicted in Fig. 4(a). It is evident that the LDD sequences, utilizing detuning-resistant phase arrangements techniques, exhibit notable state leakage and fidelity degradation when the driving power is limited. Conversely, the ZDD technique offers improved fidelity by effectively suppressing state leakage. It is noteworthy that the ZDD sequence happens to be the robust composite pulse sequence used in Ref. [19] to avoid leakage. However, instead of utilizing 3:1 duration of orthogonal phases to construct composite pulses for a π pulse, 1:1 duration should be used in the low-power limit δ', below which the π pulses cannot be implemented. In Fig. 4(b), the minimum driving power needed for LDD sequences to reach 0.99 fidelity for different pulse intervals are simulated. While the LDD methods can achieve higher fidelity by increasing power as long as the rotating-wave approximation is valid, the ZDD approach exhibits a notable advantage in quantum sensing tasks with limitations on microwave power intensity and stability.

We further analyze the mechanisms for this result from the perspective of the filter functions (FFs). Measurements of the FFs $F(t,\omega)$ of different DD sequences at

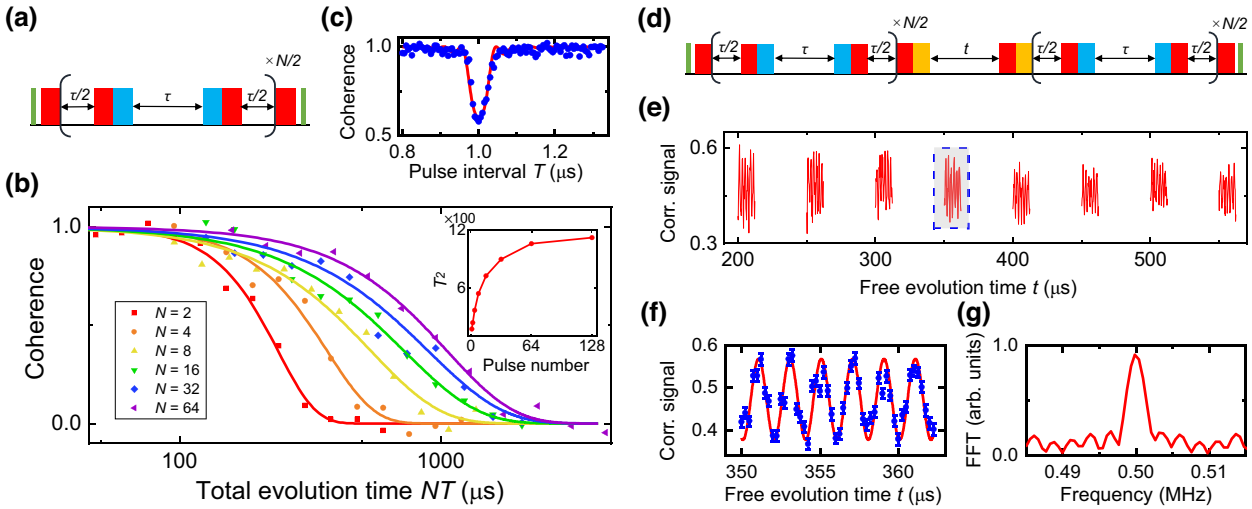

FIG. 3. Zero-field decoherence measurements and correlation spectroscopy. (a) The ZDD-N sequence. The red and blue rectangles represent U_0 and U_π operations, respectively. (b) Decoherence measurements under ZDD-N sequences. The inset depicts the coherence saturation as the pulse number increases, ranging from the DQ spin echo to the ZDD-128 sequence. (c) ac signal measurement with the ZDD-64 sequence. The coherence dip is fitted by a fluctuating magnetic field of strength $B_{\mathrm{RMS}} = 24.3(5)$ nT with $T_s = 1.002(1)$ μs. (d) The zero-field correlation spectroscopy sequence. The yellow rectangles represent the $U_{\pi/2}$ operations. (e) ac signal measurement with the correlation spectroscopy sequence. The phases accumulated during two ZDD-16 sequences with $\tau = T_s - 2T'$ are correlated. (f) The data of the boxed gray area shown in (e). Correlation data (blue dots) are fitted by a 0.5-MHz sinusoidal oscillation (red line). (g) The discrete Fourier transform of the correlation data in (e).

$\omega = 0.5$ MHz are presented in Fig. 4(c). When the driving powers are increased, the signal filtering of both the LDD and OC sequences becomes better. However, the ZDD sequence operating with the low-power limit $\Omega = \delta'$ exhibits a reasonable lineshape. To quantify the similarity between the ZDD FF and the ideal FF, we define the FF similarity as $(\int F_{\mathrm{ZDD}}(t,\omega)\,\mathrm{d}t/\int F_{\mathrm{ideal}}(t,\omega)\,\mathrm{d}t)$. A higher value of the FF similarity indicates that the ZDD FF more closely approaches the desired characteristics of the ideal FF. The fact that the FF similarity is less than 1 is primarily caused by the finite duty cycle of the manipulating pulses. Nonetheless, the FF simulation is above 0.99 when the duty cycle is lower than 20% [Fig. 4(d)]. In practice, the nondegenerate splitting δ' can be controlled by applying transverse strains, allowing for an adjustable duty cycle.

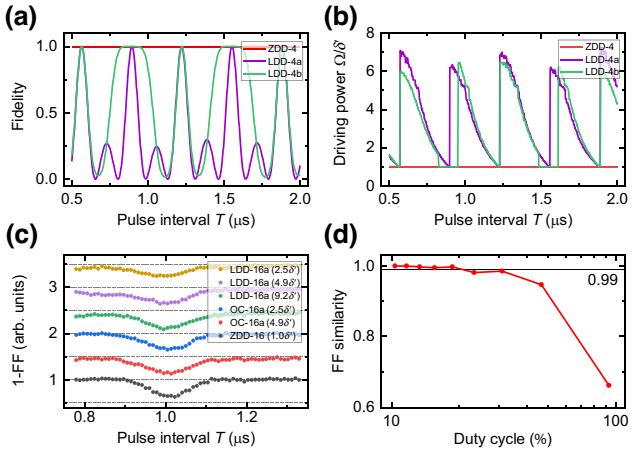

FIG. 4. Comparison of ZDD and high-power DD sequences. (a) Fidelity of DD sequences with different pulse intervals under the same driving power. (b) The minimum power needed for 0.99 fidelity of DD sequences with different pulse intervals. (c) Measurements of the FFs at $\omega = 0.5$ MHz. (d) Similarity for the ZDD-16 FFs with respect to the ideal FFs under different duty cycles.

VI. DISCUSSION AND CONCLUSION

We introduce a precise geometric control protocol and demonstrate its application in a zero-field quantum sensing technique. The sequences employed for dynamical decoupling and correlation spectroscopy are specifically designed using phased geometric gates. Our method offers a broader range of gate operations in sequence design, enabling arbitrary unitary operations within the subspace spanned by the 3LS dynamical states. The method also prevents the detrimental effects of state leakage with relatively small pulse amplitude by utilizing the properties of the geometric phase. In practice, the maximum manipulating power is not only set by the efficiency of the microwave transmission and the rotating-wave approximation, but also is limited by the vulnerabilities of the systems under measurement, where the effects of distortion and heating caused by strong electromagnetic field are not negligible.

In addition to the N-V center, other solid spin systems such as divacancies in SiC [28] offer more alternatives for implementing the DQ manipulations with phased geometric gates. These systems possess a nondegenerate splitting that can be easily adjusted by strains or electric fields, enabling precise operations even with a short dephasing time. This allows for a broadened sensing bandwidth and the analysis of electric field noise. Furthermore, it is worth noting that in the absence of the hyperfine interaction, our protocol can be extended to the low-field regime, as long as the 3LS configuration is maintained, thereby expanding its potential applications in various quantum technologies.

ACKNOWLEDGMENTS

This work was supported by the National Natural Science Foundation of China (Grant No. T2125011), the CAS (Grant No. GJJSTD20200001,YSBR-068), Innovation Program for Quantum Science and Technology (Grant No. 2021ZD0302200,2021ZD0303204), the Anhui Initiative in Quantum Information Technologies (Grant No. AHY050000), and the Fundamental Research Funds for the Central Universities, New Cornerstone Science Foundation through the XPLORER PRIZE.

This work was partially carried out at the USTC Center for Micro and Nanoscale Research and Fabrication.

APPENDIX A: DERIVATION OF THE PHASED GEOMETRIC GATES

In the rotating frame governed by

$$H_0^{(1)} = \omega S_z^2. \tag{A1}$$

The system Hamiltonian in Eq. (1) turns into

$$H' = U_0^{(1)}(t)^\dagger H U_0^{(1)}(t) + i(\partial_t U_0^{(1)}(t)^\dagger) U_0^{(1)}(t), \tag{A2}$$

where $U_0^{(1)}(t) = \exp(-iH_0^{(1)}t)$. Tuning the system into resonance with $\omega = D + d_\parallel \Pi_z$ and applying the rotating-wave approximation (valid when $\Omega/\omega \ll 1$ is satisfied), the Hamiltonian becomes

$$H' \approx \begin{bmatrix} \delta/2 & \Omega e^{-i\phi}/2\sqrt{2} & -id_\perp \Pi_y \\ \Omega e^{i\phi}/2\sqrt{2} & 0 & \Omega e^{i\phi}/2\sqrt{2} \\ id_\perp \Pi_y & \Omega e^{-i\phi}/2\sqrt{2} & -\delta/2 \end{bmatrix}. \tag{A3}$$

With the $\{|+\rangle, |0\rangle, |-\rangle\}$ basis, the Hamiltonian in Eq. (A3) can be written as

$$H_1(\Omega, \phi) = \begin{bmatrix} 0 & \Omega e^{-i\phi}/2 & \delta' e^{-i\psi}/2 \\ \Omega e^{i\phi}/2 & 0 & 0 \\ \delta' e^{i\psi}/2 & 0 & 0 \end{bmatrix}, \tag{A4}$$

where $\delta' = \sqrt{\delta^2 + 4d_\perp^2 \Pi_y^2}$ and $\psi = \arctan(-2d_\perp \Pi_y/\delta)$. When the resonance condition $\Omega = \delta'$ is met, complete transition between the states $|0\rangle$ and $|-\rangle$ can be realized. The π operation of $\{|0\rangle, |-\rangle\}$ subspace defined by ϕ can be written explicitly as

$$U_\phi = \exp(-iH_1(\delta', \phi)T') = \begin{bmatrix} -1 & 0 & 0 \\ 0 & 0 & -e^{i(\phi-\psi)} \\ 0 & -e^{-i(\phi-\psi)} & 0 \end{bmatrix}, \tag{A5}$$

where $T' = \sqrt{2}\pi/\Omega$ is a half-period of the $|0\rangle \leftrightarrow |-\rangle$ transition or a total period of the $|0\rangle \leftrightarrow |+\rangle$ transition. As a result, U_ϕ operation adds a geometric π phase to the $|+\rangle$ state, and the pair $G_\theta = U_\phi U_{\phi+\theta}$ is represented in the $\{|+\rangle, |0\rangle, |-\rangle\}$ basis as

$$G_\theta = \begin{bmatrix} 1 & 0 & 0 \\ 0 & e^{-i\theta} & 0 \\ 0 & 0 & e^{i\theta} \end{bmatrix}. \tag{A6}$$

In the $\{|+\rangle, |-\rangle\}$ subspace, the G_θ operation allows for the implementation of arbitrary rotation around the z axis within the Bloch sphere defined by the $\{|+\rangle, |-\rangle\}$ basis. Note that the free evolution rotates the state vector along the horizontal axis, therefore, arbitrary effective rotation in the $\{|+\rangle, |-\rangle\}$ subspace can be implemented by combining free evolutions and phased geometric gates.

APPENDIX B: EFFECTS OF LARGE NONDEGENERATE SPLITTINGS

In solid spin systems, the strength of the transverse electric dipole interaction in Eq. (1) can often be significant. This can pose challenges when attempting to perform double quantum transition DD methods, as the required Rabi frequency becomes too large to satisfy the rotating-wave approximation. As a result, the performance of the DD sequences can be degraded under such circumstances (Fig. 5), highlighting the advantages of low-power methods. Compared with the LDD sequence that requires strong driving power to mitigate detuning effects, the ZDD operation with moderate driving power is more applicable to systems characterized by large nondegenerate splittings.

APPENDIX C: GATE FIDELITY WITH LIMITED DEPHASING TIME

To evaluate the impact of N-V center T_2^* on our protocol, we conduct a simulation that assessed the performance of a geometric gate pair in the presence of quasistatic noise characterized by a Gaussian distribution (Fig. 6). The result shows that when the dephasing time T_2^* exceeds 3 μs, the fidelity of the G_π gate can exceed 0.995. For a single phased geometric gate implemented in other 3LSs, the condition for satisfactory performance is $T_2^* > 10/\delta'$.

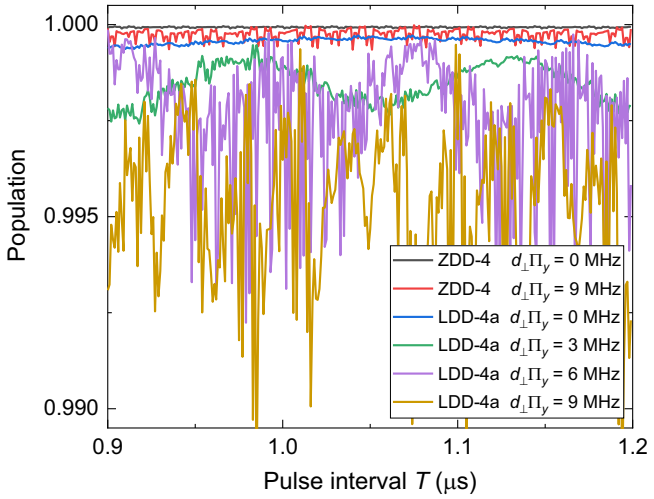

FIG. 5. DD simulations for N-V center with different levels of transverse electric dipole interaction strength. Each LDD-4a sequence is simulated with a Rabi frequency that is 10 times higher than the Rabi frequency used in the corresponding ZDD sequence. For transverse electric dipole couplings of 0, 3, 6, and 9 MHz, the Rabi frequencies for the LDD-4a sequences are 31, 68, 125, and 182 MHz.

APPENDIX D: ROBUSTNESS OF THE PHASED GEOMETRIC GATES

The robustness of our method against stray detuning Δ_e and amplitude error δ_e is depicted in Fig. 7 through simulation.

Although G_θ is equivalent to a rotation operation in the $\{|+\rangle, |-\rangle\}$ subspace, the gate robustness against pulse errors varies for different initial states. This variation can be attributed to the fact that the phase change induced by the gate can be divided into two parts: a dynamical part and a geometric part. The geometric part is resistant to errors, and only the initial states on the equator of the Bloch sphere spanned by the $\{|\zeta\rangle, |\zeta_\perp\rangle\}$ basis undergo purely geometric phase change, where $|\zeta\rangle = (|+\rangle + |\phi'\rangle)/\sqrt{2}$ and $|\zeta_\perp\rangle = (|+\rangle - |\phi'\rangle)/\sqrt{2}$. These states can be expressed explicitly as $a|+\rangle + b|0\rangle + c|-\rangle + e^{id}(a|+\rangle - b|0\rangle - c|-\rangle)$, where $a, b, c \in \mathbb{C}$ and $d \in \mathbb{R}$.

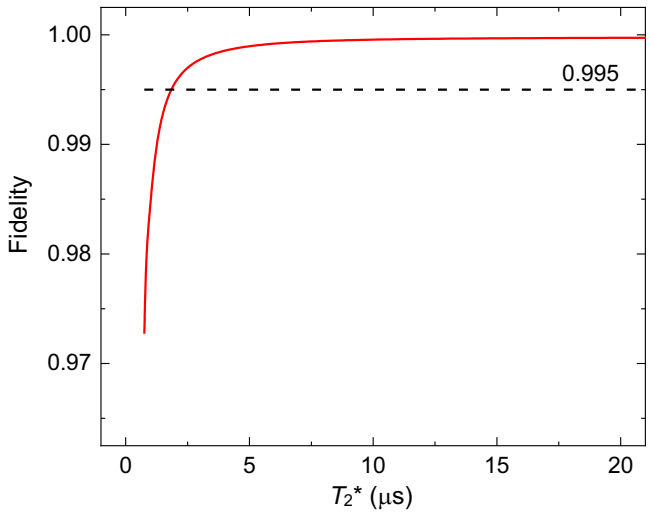

FIG. 6. Simulation of the G_π gate fidelity with limited T_2^*.

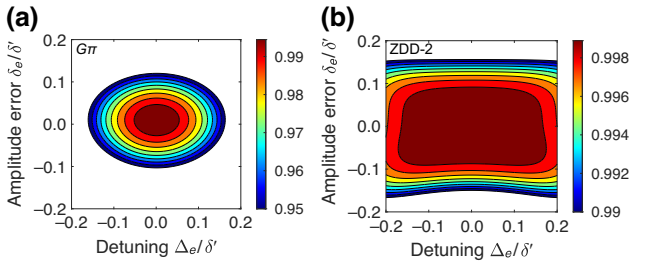

FIG. 7. Simulation of the operation with stray detuning and amplitude error. Initiate the state to $|-\rangle$, the probability of the state remains $|-\rangle$ after the gates is plotted on the z axis. (a) The G_π operation. (b) The ZDD-2 operation, the phases assigned to the U_ϕ gates in the sequence are $(0, \pi, \pi, 0)$, corresponding to the operation $G_\pi G_{-\pi}$.

The simulations of the robustness of the ZDD-4 sequence with different initial states are depicted in Fig. 8. The fidelity of the 3LS manipulation is evaluated by $F = |\mathrm{Tr}(AB^\dagger)|$, where A represents the identity and B represents the ZDD-4 propagator. In zero-field correlation spectroscopy experiment, one way to ensure the performance of sequence is mitigating detuning, another is reducing the phase accumulation period to avoid operations on the states near $|\pm 1\rangle$.

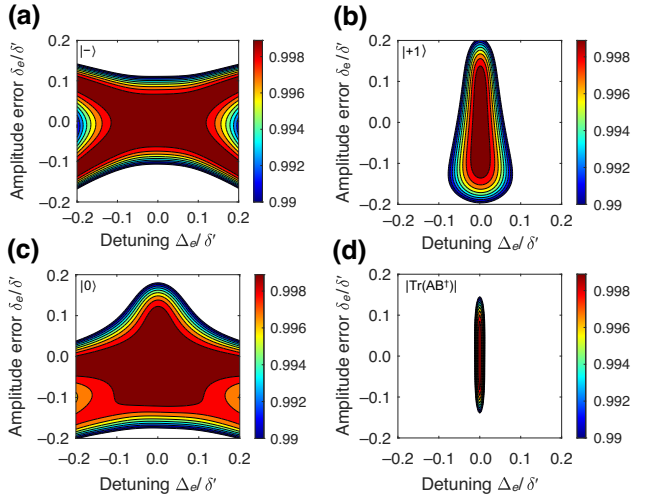

FIG. 8. Simulation of the robustness of the ZDD-4 sequence with different initial states, the phase arrangement is $(0, \pi, \pi, 0, \pi, 0, 0, \pi)$. (a) Initial state $|-\rangle$. (b) Initial state $|+1\rangle$. (c) Initial state $|0\rangle$. (d) Overall fidelity $F = |\mathrm{Tr}(AB^\dagger)|$.

In our protocol, the state is prepared to $|-\rangle$ after the first 2π pulse, ensuring the robustness of the ZDD sequences. However, in the zero-field correlation spectroscopy experiment, it becomes necessary to either reduce the phase accumulation period or mitigate pulse-detuning errors to ensure the performance of the sequence.

APPENDIX E: EXPERIMENTAL SETUP AND MEASUREMENT

We use a ^{12}C-enriched diamond chip implanted with 40 keV $^{15}N^{+}$ ions for our experiments. The top and lateral sides of the diamond chip are perpendicular to the crystal's [100] and [110] axes, respectively. To counterbalance the geomagnetic field, a set of permanent magnets is employed, reducing the field strength to below 0.005 mT. In this regime, we ensure that $\Delta/\delta << 1$, where δ is dominated by the intrinsic ^{15}N hyperfine interaction $A_{\parallel}$ for single N-V centers.

A 532-nm laser is employed to excite the single N-V centers using confocal microscopy, and we capture the fluorescence photons using avalanche photodiodes and a counter card. The microwave for N-V center manipulation is generated by a Keysight M8190A arbitrary waveform generator and amplified by a Mini-Circuits ZHL-25W-63+ high-power amplifier. We use a coplanar waveguide for microwave transmission and ensure that the transverse microwave polarization is aligned perpendicular to the transverse effective electric field vector by measuring the transition probabilities for the two transitions in Fig. 1(a) via a pulsed optically detected magnetic resonance experiment.

To mitigate the effect of relaxation, the decoherence curves depicted in Figs. 3(b) and 3(c) are measured by subtracting population in the state $|0\rangle$ after two individual sequences, one is shown in Fig. 3(a) and another is performed by inserting an additional $\pi/(2\delta')$ free evolution into the former sequence before the final 2π pulse. The quantity obtained by subtraction linearly maps the coefficient of the nondiagonal term $|+1\rangle\langle-1|$ in the $\{|+1\rangle, |0\rangle, |-1\rangle\}$ basis to the range [0,1], which corresponds to the coherence of the system.

The FFs $F(t,\omega)$ shown in Fig. 4(c) are measured by summing up the squared phases accumulated during the DD sequences in the presence of coherently oscillating external fields $B_z\cos(\omega t)$ and $B_z\sin(\omega t)$, respectively [16].

[1] J. F. Barry, J. M. Schloss, E. Bauch, M. J. Turner, C. A. Hart, L. M. Pham, and R. L. Walsworth, Sensitivity optimization for NV-diamond magnetometry, Rev. Mod. Phys. **92**, 015004 (2020).

[2] F. Dolde, H. Fedder, M. W. Doherty, T. Nöbauer, F. Rempp, G. Balasubramanian, T. Wolf, F. Reinhard, L. C. L. Hollenberg, F. Jelezko, and J. Wrachtrup, Electric-field sensing using single diamond spins, Nat. Phys. **7**, 459 (2011).

[3] G. Kucsko, P. C. Maurer, N. Y. Yao, M. Kubo, H. J. Noh, P. K. Lo, H. Park, and M. D. Lukin, Nanometre-scale thermometry in a living cell, Nature **500**, 54 (2013).

[4] L. M. Pham, S. J. DeVience, F. Casola, I. Lovchinsky, A. O. Sushkov, E. Bersin, J. Lee, E. Urbach, P. Cappellaro, H. Park, A. Yacoby, M. Lukin, and R. L. Walsworth, NMR technique for determining the depth of shallow nitrogen-vacancy centers in diamond, Phys. Rev. B **93**, 045425 (2016).

[5] M. S. J. Barson, P. Peddibhotla, P. Ovartchaiyapong, K. Ganesan, R. L. Taylor, M. Gebert, Z. Mielens, B. Koslowski, D. A. Simpson, L. P. McGuinness, J. McCallum, S. Prawer, S. Onoda, T. Ohshima, A. C. Bleszynski Jayich, F. Jelezko, N. B. Manson, and M. W. Doherty, Nanomechanical sensing using spins in diamond, Nano Lett. **17**, 1496 (2017).

[6] A. M. Thayer, J. M. Millar, and A. Pines, Two-dimensional zero-field NMR and NQR, Chem. Phys. Lett. **129**, 55 (1986).

[7] A. M. Thayer and A. Pines, Zero-field NMR, Acc. Chem. Res. **20**, 47 (1987).

[8] D. A. Barskiy, M. C. D. Tayler, I. Marco-Rius, J. Kurhanewicz, D. B. Vigneron, S. Cikrikci, A. Aydogdu, M. Reh, A. N. Pravdivtsev, J.-B. Hövener, J. W. Blanchard, T. Wu, D. Budker, and A. Pines, Zero-field nuclear magnetic resonance of chemically exchanging systems, Nat. Commun. **10**, 3002 (2019).

[9] A. I. Ahonen, M. S. Hämäläinen, M. J. Kajola, J. E. T. Knuutila, P. P. Laine, O. V. Lounasmaa, L. T. Parkkonen, J. T. Simola, and C. D. Tesche, 122-channel squid instrument for investigating the magnetic signals from the human brain, Phys. Scr. **T49A**, 198 (1993).

[10] R. Fenici, D. Brisinda, and A. M. Meloni, Clinical application of magnetocardiography, Expert Rev. Mol. Diagn. **5**, 291 (2005).

[11] Y. Wei, W. Zhang, B. Lv, X. Xu, S. Xi, and Z. Ma, Ultralow magnetic damping of a common metallic ferromagnetic film, Sci. Adv. **7**, eabc5053 (2021).

[12] I. Lovchinsky, A. O. Sushkov, E. Urbach, N. P. de Leon, S. Choi, K. De Greve, R. Evans, R. Gertner, E. Bersin, C. Muller, L. McGuinness, F. Jelezko, R. L. Walsworth, H. Park, and M. D. Lukin, Nuclear magnetic resonance detection and spectroscopy of single proteins using quantum logic, Science **351**, 836 (2016).

[13] I. Lovchinsky, J. D. Sanchez-Yamagishi, E. K. Urbach, S. Choi, S. Fang, T. I. Andersen, K. Watanabe, T. Taniguchi, A. Bylinskii, E. Kaxiras, P. Kim, H. Park, and M. D. Lukin, Magnetic resonance spectroscopy of an atomically thin material using a single-spin qubit, Science **355**, 503 (2017).

[14] H. Zheng, J. Xu, G. Z. Iwata, T. Lenz, J. Michl, B. Yavkin, K. Nakamura, H. Sumiya, T. Ohshima, J. Isoya, J. Wrachtrup, A. Wickenbrock, and D. Budker, Zero-field magnetometry based on nitrogen-vacancy ensembles in diamond, Phys. Rev. Appl. **11**, 064068 (2019).

[15] T. Lenz, A. Wickenbrock, F. Jelezko, G. Balasubramanian, and D. Budker, Magnetic sensing at zero field with a single nitrogen-vacancy center, Quantum Sci. Technol. **6**, 034006 (2021).

[16] J. Cerrillo, S. Oviedo Casado, and J. Prior, Low field nano-NMR via three-level system control, Phys. Rev. Lett. **126**, 220402 (2021).
[17] Y. Sekiguchi, Y. Komura, S. Mishima, T. Tanaka, N. Niikura, and H. Kosaka, Geometric spin echo under zero field, Nat. Commun. **7**, 11668 (2016).
[18] Y. Sekiguchi, Y. Komura, and H. Kosaka, Dynamical decoupling of a geometric qubit, Phys. Rev. Appl. **12**, 051001 (2019).
[19] P. J. Vetter, A. Marshall, G. T. Genov, T. F. Weiss, N. Striegler, E. F. Grossmann, S. Oviedo-Casado, J. Cerrillo, J. Prior, P. Neumann, and F. Jelezko, Zero- and low-field sensing with nitrogen-vacancy centers, Phys. Rev. Appl. **17**, 044028 (2022).
[20] M. H. Abobeih, J. Randall, C. E. Bradley, H. P. Bartling, M. A. Bakker, M. J. Degen, M. Markham, D. J. Twitchen, and T. H. Taminiau, Atomic-scale imaging of a 27-nuclear-spin cluster using a quantum sensor, Nature **576**, 411 (2019).
[21] J. Smits, J. T. Damron, P. Kehayias, A. F. McDowell, N. Mosavian, I. Fescenko, N. Ristoff, A. Laraoui, A. Jarmola, and V. M. Acosta, Two-dimensional nuclear magnetic resonance spectroscopy with a microfluidic diamond quantum sensor, Sci. Adv. **5**, eaaw7895 (2019).
[22] Z. Yang, X. Kong, Z. Li, K. Yang, P. Yu, P. Wang, Y. Wang, X. Qin, X. Rong, C. Duan, F. Shi, and J. Du, Structural analysis of nuclear spin clusters via 2D nanoscale nuclear magnetic resonance spectroscopy, Adv. Quantum Technol. **3**, 1900136 (2020).
[23] P. Jamonneau, M. Lesik, J. P. Tetienne, I. Alvizu, L. Mayer, A. Dreau, S. Kosen, J.-F. Roch, S. Pezzagna, J. Meijer, T. Teraji, Y. Kubo, P. Bertet, J. R. Maze, and V. Jacques, Competition between electric field and magnetic field noise in the decoherence of a single spin in diamond, Phys. Rev. B **93**, 024305 (2016).
[24] Y. Aharonov and J. Anandan, Phase change during a cyclic quantum evolution, Phys. Rev. Lett. **58**, 1593 (1987).
[25] A. M. Souza, G. A. Álvarez, and D. Suter, Robust dynamical decoupling, Philos. Trans. R. Soc. **370**, 4748 (2012).
[26] G. T. Genov, D. Schraft, N. V. Vitanov, and T. Halfmann, Arbitrarily accurate pulse sequences for robust dynamical decoupling, Phys. Rev. Lett. **118**, 133202 (2017).
[27] A. Laraoui, F. Dolde, C. Burk, F. Reinhard, J. Wrachtrup, and C. A. Meriles, High-resolution correlation spectroscopy of 13C spins near a nitrogen-vacancy centre in diamond, Nat. Commun. **4**, 1651 (2013).
[28] W. F. Koehl, B. B. Buckley, F. J. Heremans, G. Calusine, and D. D. Awschalom, Room temperature coherent control of defect spin qubits in silicon carbide, Nature **479**, 84 (2011).